Published in final edited form as:
Invest Ophthalmol Vis Sci. 2010 March ; 51(3): 1464–1474. doi:10.1167/iovs.09-3984.

A Comparison of Optic Nerve Head Morphology Viewed by Spectral Domain Optical Coherence Tomography and By Serial Histology

NG Strouthidis[1], **J Grimm**[1], **GA Williams**[1], **GA Cull**[1], **DJ Wilson**[2], and **CF Burgoyne**[1]

[1] Optic Nerve Head Research Laboratory, Devers Eye Institute, Legacy Health System, Portland, Oregon, USA

[2] Casey Eye Institute, Oregon Health & Science University, Portland, Oregon, USA

Abstract

PURPOSE—To compare serial optic nerve head (ONH) histology with interpolated B-scans generated from a three-dimensional (3D) spectral domain OCT (SD-OCT) ONH volume acquired in vivo from the same normal monkey eye.

METHODS—A 15°, ONH SD-OCT volume was acquired in a normal monkey eye, with IOP controlled at 10 mmHg, using the Heidelberg Spectralis. Following perfusion fixation at 10 mmHg, the ONH was trephined, embedded in a paraffin block and sagittal sections were cut at 4 μm intervals. The location of each section was identified within the optic disc photograph by matching the position of the retinal vessels and of Bruch's membrane opening. By altering the angles of rotation and incidence, "interpolated" B-scans matching the location of the histologic sections were generated using custom software. Structures identified in the histologic sections were compared to signals identified in matched B-scans.

RESULTS—Close matches between histologic sections and interpolated B-scans were identified throughout the extent of the ONH. SD-OCT identified the neural canal opening as the termination of the Bruch's membrane/retinal pigment complex and Border Tissue as the innermost termination of the choroidal signal. The anterior lamina cribrosa and its continuity with the prelaminar glial columns were also detected.

CONCLUSIONS—Volumetric SD-OCT imaging of the ONH was capable of generating interpolated B-scans which accurately matched serial histologic sections. In this single monkey ONH, SD-OCT captured the anterior laminar surface, which is likely to be a key structure in the detection of early ONH structural damage in ocular hypertension and glaucoma.

The application of optical coherence tomography (OCT) technology in clinical glaucoma practice has largely centered on imaging the peripapillary retinal nerve fiber layer. This approach has shown promise, both in assisting the clinician in diagnosing glaucoma and also in detecting disease progression.[1–6] There is mounting evidence to suggest that the primary site of injury to the retinal ganglion cell axon is at the level of the lamina cribrosa.[7–12] An ability to image the lamina cribrosa, and other structures deep within the optic nerve head (ONH), would therefore constitute a major advance. Indeed, recent work using post-mortem

---

Address for Reprints: Claude F. Burgoyne, MD, Optic Nerve Head Research Laboratory, Devers Eye Institute, 1225 NE 2nd Ave, PO Box 3950, Portland OR 97208-3950. cfburgoyne@deverseye.org.

Commercial Disclosure: NGS is funded by an unrestricted educational grant from Heidelberg Engineering and by a Royal College of Ophthalmologists/Pfizer Fellowship; CFB receives instrument and unrestricted research support but no honoraria or consultant funds from Heidelberg Engineering.

three dimensional (3D) histomorphometric ONH reconstructions has identified a number of ‘cardinal’ morphological changes at the earliest stage of experimental glaucoma.[13–16] These changes include a thickening of the prelaminar tissue (as distinct from the thinning one would expect to observe at the later stages of the neuropathy), posterior deformation and thickening of the lamina cribrosa and expansion of the scleral canal. We propose that the identification of these changes in vivo may help to identify those eyes with the earliest signs of distress in response to an IOP-mediated insult, and as such at high risk of future functional damage.

The ability of OCT to image retinal morphology has been validated by a number of seminal studies which have sought to compare OCT tomograms to conventional serial histology in humans,[17, 18] non-human primate,[19–21] tree shrew,[22] rodent [23] and pig species.[24] Although not the principal aim, a number of these studies also included brief comments pertaining to ONH and peripapillary retinal morphology.[21, 22, 24] Besides these commentaries, there have not been, to date, any formal, rigorous comparisons of ONH morphology as imaged by OCT and by light microscopy. An obvious reason for this is that the axial (depth) resolution of conventional time domain OCT (approximately 10 μm) has not been sufficient for resolving structures deep to the surface of the optic disc cup. With the commercial introduction of spectral domain OCT (SD-OCT), which has both an improved axial resolution (approaching 5 μm) and vastly increased acquisition speed, the 3D detection of deep ONH targets has become tangible.

A number of recent reports suggest that SD-OCT imaging of the human ONH can capture the lamina cribrosa.[25, 26] Whilst these reports are encouraging, it is essential that the SD-OCT’s ability to capture deep ONH targets be validated by comparison with conventional serial histology. The purpose of this study was to compare interpolated SD-OCT B-scans generated from a volumetric SD-OCT reconstruction acquired in vivo from a normal monkey ONH with serial histologic sections obtained post mortem from the same ONH. This study required the development of a novel method of generating ‘tailor-made’ interpolated B-scans in any orientation from the 3D SD-OCT volume. This method is also fully described.

METHODS

Optic Nerve Head Imaging

This study was performed on the left eye of a 6.8 year old, 4.5 kg female rhesus macaque (*Macaca mulatta*). The local Institutional Animal Care and Use Committee (Legacy Health System, Portland, OR) approved this study and the subject animal was treated in accordance with the ARVO statement for the use of animals in ophthalmic and vision research.

In vivo imaging with a rigid plano contact lens placed onto the corneal surface was performed immediately prior to sacrifice. The animal was anesthetized using ketamine and isoflurane and the pupil was dilated with one drop each of 1% tropicamide, 2.5% phenylephrine hydrochloride and 2% cyclopentolate hydrochloride. The intraocular pressure (IOP) was adjusted to 10 mmHg using a manometer connected to a 27-gauge cannula, which was inserted into the temporal anterior chamber. After 30 minutes at an IOP of 10 mmHg, an experienced technician (GAW) acquired a pair of left optic disc stereophotographs using a simultaneous stereo fundus camera (TRC-WT Retinal Camera, Topcon, Paramus, NJ).

SD-OCT imaging of the left ONH was performed using a commercially available device (Spectralis, Heidelberg Engineering, Heidelberg, Germany). For the purposes of this study a horizontal raster scan pattern was acquired with 290 individual horizontal B-scans, 768 A-scans per B-scan, and with each B-scan acquired 9 times and averaged for speckle noise reduction. The scan was centered on the ONH, using a 15° retinal window. The device’s in-built eye tracking facility was turned on during acquisition. The device’s native viewing software automatically registered all consecutive B-scans relative to each other in the z-axis.

Animal Sacrifice During Perfusion Fixation

At the conclusion of imaging, the animal was killed during perfusion fixation through the descending aorta with 1 L of 4% buffered hypertonic paraformaldehyde solution followed by 6 L of 5% buffered hypertonic gluteraldehyde solution. IOP was maintained at 10 mmHg for 1 hour, after which the left orbital contents were exenterated via a lateral orbitotomy. All orbital tissue was immediately removed from the globe. The anterior chamber was removed 2 to 3 mm posterior to the limbus and the posterior scleral shell with intact optic nerve, ONH, choroid and retina was placed in 5% glutaraldehyde for storage.

Tissue Preparation

The optic nerve was removed leaving a 3mm stump attached to the globe. The ONH and peripapillary sclera were trephined (6 mm in diameter, passed from the vitreous surface through the sclera) and a triangular notch was cut into the superior peripapillary sclera. The trephine was photographed at X2 magnification using using an SLR camera (FM2, Nikon, Tokyo) attached to a dissecting microscope (Stereomaster, Thermo Fisher Scientific Inc, Waltham, MA).

Co-localization of the SD-OCT Infra-Red Image to the ONH Trephine Image (Figure 1)

In order to generate histologic sections at approximately the same orientation as the acquired SD-OCT B-scans, the location of the 15 degree SD-OCT acquisition window was overlaid onto the digital ONH trephine image. Firstly, the 35 mm color slide image of the trephine was digitized at a resolution of 4800 dpi using a color-calibrated scanner (ArtixScan M1 Slide Scanner, Microtek Lab, Inc., Fontana, CA). The SD-OCT infra-red (IR) image was then overlaid onto the digitized ONH trephine image using commercially available image processing software (Adobe Photoshop CS3, Adobe Systems, Inc., San Jose, CA) by matching the central retinal vessels and their bifurcations. Figure 1A shows the co-localized IR image, including the SD-OCT acquisition box, at 50% opacity, overlying the ONH trephine photograph. In Figure 1B, the co-ordinates of the SD-OCT acquisition box have been burnt onto the ONH trephine image.

Tissue Embedding

Three attempts were made to cut the inferior edge of the ONH trephine under the dissecting microscope parallel to the inferior boundary of the co-localized acquisition box. This was performed using a single edged number 12 industrial razor blade (VWR, West Chester, PA) whilst referencing the image shown in Figure 1B. After each cut the ONH trephine was re-photographed and the resultant digital image co-localized to Figure 1B so as to assess the accuracy of the cut relative to the inferior border of the overlaid acquisition box. After each inferior cut was found to be inaccurate, two additional cuts were made to the superior trephine, the second of which best approximated the desired orientation (Figure 1C). The trephine was then embedded in paraffin using standard histologic technique, with the superior cut surface facing downwards in the block.

Histologic Sectioning and Staining

The ONH specimen block was sectioned at 4 μm intervals using a microtome (RM 2155, Leica Biosystems, St Louis, MO). Sections were floated in a water bath (56° C) and picked up onto slides which were incubated overnight at 60° C. Prior to staining, slides were deparaffinized through two changes of xylene for 5 minutes. The slides were then hydrated through two changes each of absolute alcohol and 95% alcohol followed by one change of 70% alcohol and then rinsed in running tap water.

Every fourth section (16 μm intervals) was stained with hematoxylin and eosin (HE) by immersion for 4 minutes in Shandon's Instant Hematoxylin (Thermo-Fisher Scientific, Inc.) then rinsed in running tap water for 5 minutes, counterstained for 45 seconds in eosin, dehydrated, then mounted with a synthetic medium (Eukitt).

In addition to the HE stained slides, individual unstained slides from regions of interest within the ONH were selected for alternative staining (all stains acquired from Thermo-Fisher Scientific, Inc.). For Masson Trichrome (MT) staining, the deparaffinized, hydrated slides were immersed in Weigert's Hematoxylin for 10 minutes then rinsed in running water for 10 minutes. The slides were then immersed in Biebrich Scarlet-Acid Fuchsin for 5 minutes, then rinsed in distilled water. Finally the slides were immersed in phosphomolybdic-phosphotungstic acid solution for 10 minutes and aniline blue solution for 3 minutes. The slides were rinsed in distilled water, immersed in 1% glacial acetic acid, dehydrated, cleared then mounted. Burke's modification for the combined staining of cells and fibers in the nervous system was used to achieve Luxol Fast Blue/Cresyl Violet Acetate (LFB) staining.[27] Finally, staining with a 1:1 (vol/vol) mixture of ponceau-saffron and acid fuchsin was performed in a few selected slides as this is the connective tissue stain used in our 3D histomorphometric reconstruction technique.[12, 15, 16]

Slides selected for comparison with SD-OCT B-scans were imaged at 10X magnification using an inverted microscope (Leica DM IRBE) and image capture software (Bioquant Life Science, Version 8.10.20, Bioquant Image Analysis Corporation, Nashville, TN).

Orientation of Histologic Sections Relative to The Optic Disc Photograph (Figure 2)

The 35 mm color stereo slide pair was digitized as outlined for the trephine photo, above. The HE-stained sections (every fourth section) were then reviewed to identify in which slides the superior and inferior openings in the retinal pigment epithelium (RPE) and Bruch's membrane were present. These slides therefore served as 'cardinal' orientation slides, corresponding to the superior and inferior disc margin on the clinical disc photograph.[28] The angle of rotation at which each section was acquired was ascertained by tracking the location of each major retinal vessel, its spacing relative to other vessels and relative to the boundaries of the optic nerve and then referencing to a location on the clinical photograph consistent with these anatomic relationships. The 'clinical' location of each histologic section was then marked onto the disc photograph, which was then co-localized/aligned to the en face SD-OCT image, using the method described above.

Generation of Interpolated B-Scans for Comparison with Serial Histology (Figure 3)

Having taken steps to ensure a close match between the histologic sections and the acquired SD-OCT B-scans, we then attempted to 'fine tune' the accuracy of the match by correcting for two sources of discrepancy. Firstly, we corrected for the degree by which the angle of rotation of the histologic section differed from that of the acquired B-scan. Secondly, we corrected for the degree by which the angle of incidence of the microtome blade and the angle of incident light from the SD-OCT device might differ. To do so, we developed a method of extracting 'interpolated' B-scans, at any angle of rotation and incidence, from the data contained within the 3D ONH SD-OCT volume (Figure 3).

Custom software, based on the Visualization Toolkit (VTK, Clifton Park, NY), was used to generate a B-scan plane (x-z plane) and to rotate it about the z-axis to reproduce the 'en face' angle of rotation. The B-scan plane was then rotated about the x-axis to reproduce the angle of incidence. These manipulations were translated to a specified point within the 3D SD-OCT volume onto which a fine grid of 1 × 1 μm squares were overlaid. The application of this fine grid onto the B-scan plane was designed to overcome the distortion from the misalignment of the plane with the volume occurring at the sub-pixel level. The fine grid squares were used to sample the volume using a nearest neighbor technique, whereby the distance of the centroid of the square in the plane to the centroids of the pixels in the volume was computed and the value from the pixel in the volume with the shortest centroid to centroid distance was selected. These data were saved as a floating point tiff image and the plane was shifted along its normal until a complete family of interpolated B-scans was generated. This software could alter the angle of rotation and incidence by 0.5° increments.

The method by which the interpolated B-Scan angle of rotation was decided for each histologic section is illustrated in Figure 4. The disc photograph, containing the topographical location of the HE-stained sections (4A) was co-localized to the en face SD-OCT image, using the method described above. Using a fixed center of rotation, the angle of rotation of each histologic section was calculated with reference to the horizontal raster acquistion box, in which the vertical axis is 0° and the horizontal axis is 90°. Having identified the angle of rotation, the purpose-built software generated the complete series of interpolated B-scans for that angle, as though the acquisition window had shifted to the selected angle of orientation.

Once the optimum angles of rotation had been identified, the angle of incidence was estimated. The interpolated B-scans generated above, using an angle of incidence of 0° (perpendicular to the imaged surface), were compared to the histologic sections from the same topographic locations. The angle of incidence was then varied by 0.5° increments until the interpolated B-scans best matched the histologic section at each location. An example demonstrating the effect of varying the angle of incidence is shown in Figure 5.

Comparison of Histologic Sections to Matched Interpolated B-scans

Matched interpolated B-scans (defined to be best corrected for angle of rotation and incidence) and their histologic sections were then qualitatively compared to identify which structures within the ONH could be identified by SD-OCT. In order to facilitate this, an attempt was made to align ONH structures within each B-scan with their respective location within the matched histologic section. Alignment was performed using image processing software (Adobe Photoshop CS3, Adobe Systems, Inc., San Jose, CA). Rotation and scaling in a 1:1 ratio were performed. We did not warp or morph images to correct for tissue processing artifacts in the histologic sections such as differential horizontal or vertical shrinkage, choroidal expansion and retinal elevation.

RESULTS

Topographic Location of Histologic Sections

525 histologic sections, with a minimum separation of 4 μm between each section, were generated from the ONH trephine. Figure 4A illustrates the location of the initial HE-stained sections (every fourth section) throughout the full extent of the disc photograph. HE-stained sections in which the retina was insufficiently preserved to allow the accurate identification of retinal vessels were not used for comparison.

Generation of Matched Interpolated B-scans

Histologic sections in the superior part of the nerve (region 1 in Figure 4C) required interpolated SD-OCT B-Scans to be generated at an angle of rotation of 73.5°. Inferior to this, there was a small portion of the nerve (region 2 in Figure 4C) in which the matched angle of rotation was 87°. The remaining sections (region 3 in Figure 4C) required an angle of 89°, which was almost identical to the acquired B-Scan angle of 90°.

The effect of altering the angle of incidence of the interpolated B-scan for a given histologic section is illustrated in Figure 5 for Section 145, which is located close to the superior disc margin. In this section the retinal pigment epithelium (RPE) and Bruch's membrane are still intact, although there is an opening in both the choroid and the sclera. An interpolated B-scan generated at an angle of incidence of 0°, perpendicular to the retinal surface, (Figure 5B) was not as accurate as an interpolated B-scan generated at an angle of incidence of −18°, which was angled towards the nerve (Figure 5C).

Figure 6A shows histologic section 335, which is located close to the inferior disc margin. In this section, an opening in the choroidal space is present below the intact RPE. A very small portion of the optic nerve is visible above a small intact portion of peripapillary sclera, suggesting that the section was acquired at a less oblique angle than section 145. Figure 6B shows the matched interpolated B-scan, generated at an angle of incidence of 0°. All of the major vessels seen in the histologic section are detectable in this interpolated B-scan. Likewise the opening in the choroid is present, along with a faintly continuous RPE/Bruch's membrane complex signal. It should be noted that the shadow cast by the presence of two large retinal vessels above this region would have contributed to the 'faintness' of this latter signal. The sclera is not detected in this section, although there is a faint signal below the choroidal opening suggesting that some reflected light from the underlying optic nerve has been captured.

An angle of incidence of −18° was found to achieve the best matches in the part of the nerve where sections were acquired at an angle of rotation of 73.5° (region 1 in Figure 4C). Where the angle of rotation was 87° (region 2 in Figure 4C), an angle of incidence of −10° achieved the best matches. In the remainder of the ONH, where the angle of rotation was 89° (region 3 in Figure 4C), the best matches were achieved with an angle of incidence of 0°.

Detection of Deep Optic Nerve Head Structures

Two examiners (NGS and CFB) qualitatively compared the matches between interpolated B-scans and their respective histologic sections. The vitreal surface of the ONH was detectable by SD-OCT throughout its full extent. However, SD-OCT visualization of structures deep to the surface was poor in regions where shadows were cast by the central retinal vessels.

Interpolated B-scans matched to histologic sections acquired from the central part of the disc (sections 256 – 260) were selected for the detailed assessment of deep ONH imaging, as they had the largest continuous 'shadow free' areas either side of the central retinal vessels (Figures 7, 8 and 9). For these comparisons, the same interpolated B-scan was matched to each section because the separation between adjacent B-scans was approximately 12 – 16 μm, which was comparable to the separation between the selected histologic sections. Within these sections a prominent Bergmeister's papilla was clearly visualized within both the histologic sections and the interpolated SD-OCT B-scan.

Neural Canal Opening (Figure 7)—We have previously described the neural canal to be the passage through which retinal ganglion cell axons traverse the wall of the eye, beginning at the plane of the RPE/Bruch's membrane complex (the neural canal opening, NCO) and continuing through the choroidal and scleral portions of the canal.[28, 29] Figure 7 reports the SD-OCT correlates to the histologic components of the NCO. Here the RPE/Bruch's membrane complex is defined to be the posterior signal from the hyper-reflective 'triple stripe' below the dark, hypo-reflective outer nuclear layer,[29, 30] We have previously defined the innermost termination of this signal at either side of the neural canal as the NCO.[29] In Figure 7A, section 257 (HE-stained) is shown, with the temporal canal opening magnified as an inset. The retinal layers can be seen to taper downwards towards a point between the outer nuclear and photoreceptor layers (marked by black arrows). In this section, the termination of the RPE is external to the termination of Bruch's membrane and these same relationships are easily discerned within the matched interpolated B-scan (Figure 7B). Within section 260 (Figure 7C), Ponceau S stain better reveals the extension of unpigmented Bruch's Membrane beyond the RPE.

Border Tissue of Elschnig (Figure 8)—The Border Tissue is a flange or strut of connective tissue, arising from the sclera to meet Bruch's Membrane and, in doing so, acts as the junction between the innermost termination of the choroid and the adjacent retinal ganglion cell axon bundles. In Figure 8A (histologic section 258, stained with MT), the Border Tissue of Elschnig is seen at either side of the neural canal, between the sclera and Bruch's membrane. Within the matched interpolated B-scan (Figure 8B), the Border Tissue corresponds to the junction of the choroidal signal with the nerve and the heavy pigment located just below this, at the edge of the sclera. Within this matched interpolated B-scan, the anterior scleral surface is not visible.

Pre-laminar Glial Columns and The Anterior Lamina Surface (Figure 9)—The pre-laminar glial columns are most easily visualized in the HE-stained section (Section 257, Figure 9A, black arrows) where the glial nuclei are prominently stained; to a lesser extent, the connective tissue component of these columns is detectable with MT staining (Section 258, Figure 9B). These columns can be seen to commence within the neural canal at approximately the level of the NCO and the Border Tissue. The columns extend posteriorly as vertical struts until the point where they merge with the more horizontally oriented laminar beams. Vertically orientated striations within the matched interpolated B-scan (Figure 9A) appear to correspond to the prelaminar glial columns.

In Figure 9B, we define the anterior laminar surface in the histologic section to be the innermost point at which horizontally/transversely orientated connective tissue can be identified. Within the matched interpolated B-scan there appears to be a distinction between the pre-laminar glial columns (vertical striations) and the anterior laminar surface (transversely orientated signal), particularly in the nasal side of the scan. Although the precise peripheral scleral insertion of the lamina cannot be visualized in this B-scan, the anterior laminar surface signal can be seen to bend upwards towards a point below the Border Tissue on both sides of the neural canal. The posterior laminar surface (Figure 9C) was not detectable in the matched interpolated B-scan.

DISCUSSION

This study represents an important step in verifying the deep ONH imaging capabilities of SD-OCT. The following ONH targets could be identified by SD-OCT: the vitreal surface of the ONH, pre-laminar tissue, NCO, Border Tissue, choroid, pre-laminar glial columns and the anterior laminar surface. The anterior and posterior scleral surfaces, the peripheral insertion of the lamina and the posterior laminar surface were not detectable within this SD-OCT volume.

In a series of recent articles we have identified the NCO as a relatively planar, continuous structure, which underpins the disc margin in the majority of monkey eyes.[28, 29] For these reasons, and the likelihood that an automated segmentation algorithm will reliably detect the NCO, we have proposed the NCO as a suitable basis for an SD-OCT reference plane.[29] In the current study we were unable to identify a distinct signal from Bruch's membrane separate from RPE. Interestingly, it would appear that the SD-OCT defined NCO (magnified inset of Figure 7B, took into account a portion of unpigmented Bruch's membrane, extending beyond the termination of the retinal pigment epithelium (magnified inset of Figure 7C). However, in this particular SD-OCT volume, a transition point, such as an abrupt decrease in the width of the RPE/Bruch's membrane complex, was not detected.

The detection of an SD-OCT signal attributable to the Border Tissue has clinical relevance in terms of defining the optic disc margin. We have recently identified, using postmortem 3D histomorphometric reconstructions, that the underlying disc margin anatomy in the monkey eye is governed by the orientation of Border Tissue relative to Bruch's Membrane.[28] We identified two principal Border Tissue orientations. *Internally oblique* Border Tissue occurs where the Border Tissue extends from the sclera towards the neural canal to meet Bruch's membrane (the most common orientation). *Externally oblique* Border Tissue occurs where the Border Tissue extends from the sclera, away from the neural canal, to meet Bruch's membrane. This orientation, when present, is located in the temporal half of the disc. Interestingly, in his classic description of the ultrastructure of the human and monkey ONH, Anderson was unable to detect Border Tissue of Elschnig in the monkey eye.[31] A connective tissue strut, emanating from the scleral surface, is clearly visible in the MT-stained section (Figure 8A, white arrows). This structure almost certainly represents Border Tissue of Elschnig, although it is perhaps a less robust structure than in the human eye. Our study confirms that, at least in this eye, SD-OCT volumetric reconstruction appears to accurately capture the orientation of the Border Tissue relative to the sclera and Bruch's membrane.

A key finding of this study is the confirmation that SD-OCT is capable of detecting the pre-laminar glial columns and the anterior surface of the lamina cribrosa. This suggests that SD-OCT might be useful for detecting morphological changes in the pre-laminar glial columns as well as displacement of the anterior lamina. Inoue and co-workers recently identified the lamina cribrosa to be a highly reflective signal beneath the optic disc cup in horizontal SD-OCT B-scans acquired from glaucomatous or ocular hypertensive human eyes.[26] Furthermore, the distance between the anterior and posterior borders of this signal was defined as the thickness of the lamina cribrosa. Laminar thickness measurements were found to have a high interobserver reproducibility and to be significantly correlated with visual field mean deviation.

Our comparisons between serial histology and SD-OCT in this monkey eye suggest that the detection of the lamina is not so straightforward. Within this SD-OCT volume there was a distinction between the vertical striations, which likely represent the pre-laminar glial columns, and the interconnecting horizontal signal, which likely represent the horizontal laminar beams between the vertical septae. The anterior laminar 'signal' is certainly more reflective in the SD-OCT horizontal B-scans presented by Inoue and co-workers, than in the B-scans examined in the current study.[26] Likewise, in our experience, the reflectivity of the anterior laminar surface is higher in human eyes compared to monkey eyes. Laminar reflectivity appears to be further enhanced in highly myopic and glaucomatous eyes, which we assume is due to thinning of the pre-laminar neural tissue. It is also important to note that, in humans, the central retinal trunk is located nasally whereas in the monkey the trunk tends to be central (as in this study). If one assumes that laminar reflectivity is affected by the thickness of the pre-laminar tissue, it follows that the most intense signal should be observed beneath the central, deepest, part of the cup. Unfortunately, in the eye examined in this study, the signal from the center of the lamina was obfuscated by 'fringe-washout' from the main vessel trunk.

It is also important to recognize that the ocular tissues of monkeys tend to be more heavily pigmented than human eyes.[32] The heavy pigment on the surface of the anterior sclera (and indeed the peripheral lamina) of the eye examined in this study might absorb, rather than reflect, the incoming SD-OCT illumination. This may, in part, explain why there was no signal from the anterior scleral surface or from the peripheral lamina insertion.

In this one eye, using a conventional 870 nm light source, the location of the posterior laminar surface was not apparent. In the B-scans examined in this study, the laminar signal appears to 'fade' with increasing depth through the ONH volume. We cannot be certain whether this drop-off in reflectivity is due to the absence of horizontal laminar beams at the posterior laminar surface or because the posterior limit of tissue penetration has been reached. For this reason, we would exercise caution in trying to calculate in vivo laminar thickness using SD-OCT. As Inoue and co-workers have reported that their measurements of lamina thickness were correlated to mean deviation in a cross-sectional cohort,[26] the inference is that SD-OCT will detect progressive laminar thinning in glaucoma. Although this suggestion is supported by a body of literature reporting that compression of the lamina occurs at early, moderate and severe stages of glaucoma damage,[33–35] we have identified profound laminar thickening at the earliest stages of the neuropathy in a non-human primate model of glaucoma.[15] We hope that longitudinal in vivo SD-OCT ONH imaging will eventually assist in establishing the relationship between lamina morphology and stage of disease. Our confidence in identifying the posterior laminar surface may be increased with the adoption of a 1060 nm light source, which has increased axial penetration as compared to the standard 870 nm light source as used in the Spectralis.[36–38] The deep ONH imaging capabilities of this alternative light source will be verified by repeating the current experiment using a Spectralis prototype equipped with the alternative wavelength light source.

By elucidating the topographic location of the HE-stained sections with well-preserved retina, as depicted in Figure 4A, we identified that there was a clear angular discrepancy between the histologic sections and the acquired B-scans in the superior third of the ONH. It is very unlikely that the microtome rotated through successive sections to such an extent as to account for the observed discrepancy. The most likely explanation is that the retina in that region was elevated and curled upwards within the block, resulting in a ‘non-aligned’ portion of the retina contacting the microtome blade. Histologic sections in the lower two thirds of the nerve were fairly closely matched to the acquired B-scans, with only a 1° difference in the angle of rotation and the angle of incidence being perpendicular to the retinal surface. This suggests that the surface topography of the specimen was flatter and less variable in this region. The degree of retinal elevation in the ONH specimen may have been less pronounced were a larger diameter ONH trephine selected. It is also possible that the perfusion fixation process contributed to the retinal elevation by causing expansion of the choroidal space. The presence of retinal elevation in the histologic sections explains the discrepancy observed in the tilt of the anterior retinal surface in the histologic sections as compared to the interpolated B-scans, particularly in Figure 7. There is also a substantial rip in the peripapillary retina present in the nasal half of the histologic sections shown in Figures 7–9, which was likely to have further affected the degree of anterior surface tilt.

Our method of generating interpolated B-scans from the acquired SD-OCT volume represents a potentially important development in the visualization of ONH images. The matched interpolated B-scans in this report demonstrated minimal diminution in image quality compared to the acquired B-scans, despite the fairly wide variation in the angle of rotation and incidence. Greater diminution of image quality would have been observed if any of the interpolated B-scans approached a vertical orientation (perpendicular to the acquired B-scans). In the selected horizontal raster scan pattern, the x-axis contains 768 ‘samples’ per 15°, whereas the y-axis contains 290 ‘samples’ per 15°. The pixels generated are therefore not cubic but are ‘stretched’ in the y-axis, with less density of data compared to the x-axis. In order to minimize the diminution in image quality, regardless of the angle of rotation, a B-scan pattern with an equal sampling density in both axes would be required. Although it is theoretically possible to generate a 768 × 768, or indeed a 1536 × 1536, horizontal raster pattern scan using the Spectralis, achieving such a dense pattern would be limited in practical terms by the test duration and by the memory constraints of the acquisition and viewing hardware and software.

In order to achieve the best approximate alignment between the interpolated B-scans and the serial histologic B-scans, the magnitude of the B-scans was adjusted using a 1:1 scale. Although the approximate horizontal alignment appears defensible, the B-scans appear ‘stretched’ in the vertical direction, with the cup and the anterior laminar surface seemingly deeper in the B-scan as compared to the matched histologic section. The SD-OCT volumes are transferred to our custom visualization software in a 1:1 μm scale, rather than in a 1:1 pixel scale. Although the z-axis scaling is fixed, the lateral magnification (x- and y-axis orientation) of the Spectralis is based on the optics of the human and not the macaque eye. The purpose of this study was to establish the histologic basis of SD-OCT signals deep within the ONH, rather than to achieve precise structural quantification. While we are currently developing an algorithm for macaque-specific lateral magnitude scaling, that capability was beyond the scope of the current study. These scaling issues partly explain why the thicknesses of retinal layers (particularly the photoreceptor and the Bruch's Membrane/retinal pigment epithelium) appear much thicker in the interpolated B-scans than in the histologic sections. Undoubtedly there is also an effect of differential tissue shrinkage, which has not been corrected in the rescaling of the interpolated B-scans. Finally, the thicknesses seen in the deep retinal layers by SD-OCT are also likely to be influenced by the strength of reflected signal over distance, rather than just the thickness the tissue of interest.

A major limitation of this work is that it was performed on a single monkey eye, which might mean that the results not be fully applicable to all human eyes. It is also important to recognize that the optic disc examined in this study had a very regular morphology, with a distinct clinical disc margin and no evidence of tilt or of peripapillary atrophy. Indeed these latter two features are far less prevalent in monkeys than in humans, and when present usually have a less exaggerated presentation than in the human eye. However, we believe that the merits of this study are such that the results are of relevance and interest. First, the morphology and histology of the monkey and human ONH are extremely similar and as such the characterization by SD-OCT is likely to be closely matched. By using a monkey eye, we were also able to perform SD-OCT imaging immediately prior to obtaining the tissue specimen by perfusion fixation. By using an anterior chamber manometer we were able to establish the same level of IOP at the time of imaging and at the time of death. This kind of study cannot be replicated using a human eye.

This study provides histologic evidence that volumetric SD-OCT imaging of the ONH is capable of capturing ONH target structures, in particular the anterior laminar surface, which may prove useful in the detection of early changes in ocular hypertension and glaucoma.[15, 39] The novel method for generating interpolated SD-OCT B-scans at any angle of rotation or incidence will expand the clinical application of this technology in normal and glaucomatous human eyes.

Acknowledgments

The authors thank Dorothea Burke, of the Leonard Christensen Eye Pathology Laboratory, Casey Eye Institute, Portland, OR for preparation of the histologic sections.

Grant Information: R01-EY11610, Legacy Good Samaritan Foundation, Heidelberg Engineering and Sears Medical Trust

References

1. Schuman JS, Hee MR, Arya AV, et al. Optical coherence tomography: a new tool for glaucoma diagnosis. Curr Opin Ophthalmol 1995;6:89–95. [PubMed: 10150863]
2. Nouri-Mahdavi K, Hoffman D, Tannenbaum DP, Law SK, Caprioli J. Identifying early glaucoma with optical coherence tomography. Am J Ophthalmol 2004;137:228–235. [PubMed: 14962410]
3. Sihota R, Sony P, Gupta V, Dada T, Singh R. Diagnostic capability of optical coherence tomography in evaluating the degree of glaucomatous retinal nerve fiber damage. Invest Ophthalmol Vis Sci 2006;47:2006–2010. [PubMed: 16639009]

4. Budenz DL, Michael A, Chang RT, McSoley J, Katz J. Sensitivity and specificity of the StratusOCT for perimetric glaucoma. Ophthalmology 2005;112:3–9. [PubMed: 15629813]
5. Anton A, Moreno-Montanes J, Blazquez F, Alvarez A, Martin B, Molina B. Usefulness of optical coherence tomography parameters of the optic disc and the retinal nerve fiber layer to differentiate glaucomatous, ocular hypertensive, and normal eyes. J Glaucoma 2007;16:1–8. [PubMed: 17224742]
6. Wollstein G, Schuman JS, Price LL, et al. Optical coherence tomography longitudinal evaluation of retinal nerve fiber layer thickness in glaucoma. Arch Ophthalmol 2005;123:464–470. [PubMed: 15824218]
7. Gaasterland D, Tanishima T, Kuwabara T. Axoplasmic flow during chronic experimental glaucoma. 1. Light and electron microscopic studies of the monkey optic nervehead during development of glaucomatous cupping. Invest Ophthalmol Vis Sci 1978;17:838–846. [PubMed: 81192]
8. Minckler DS, Bunt AH, Johanson GW. Orthograde and retrograde axoplasmic transport during acute ocular hypertension in the monkey. Invest Ophthalmol Vis Sci 1977;16:426–441. [PubMed: 67096]
9. Quigley HA, Green WR. The histology of human glaucoma cupping and optic nerve damage: clinicopathologic correlation in 21 eyes. Ophthalmology 1979;86:1803–1830. [PubMed: 553256]
10. Quigley HA, Addicks EM, Green WR, Maumenee AE. Optic nerve damage in human glaucoma. II. The site of injury and susceptibility to damage. Arch Ophthalmol 1981;99:635–649. [PubMed: 6164357]
11. Bellezza AJ, Rintalan CJ, Thompson HW, Downs JC, Hart RT, Burgoyne CF. Deformation of the lamina cribrosa and anterior scleral canal wall in early experimental glaucoma. Invest Ophthalmol Vis Sci 2003;44:623–637. [PubMed: 12556392]
12. Burgoyne CF, Downs JC, Bellezza AJ, Hart RT. Three-dimensional reconstruction of normal and early glaucoma monkey optic nerve head connective tissues. Invest Ophthalmol Vis Sci 2004;45:4388–4399. [PubMed: 15557447]
13. Roberts MD, Grau V, Grimm J, et al. Remodeling of the Connective Tissue Microarchitecture of the Lamina Cribrosa in Early Experimental Glaucoma. Invest Ophthalmol Vis Sci 2009;50:681–690. [PubMed: 18806292]
14. Yang H, Downs JC, Bellezza AJ, Thompson H, Burgoyne CF. 3-D Histomorphometry of the Normal and Early Glaucomatous Monkey Optic Nerve Head: Prelaminar Neural Tissues and Cupping. Invest Ophthalmol Vis Sci 2007;48:5068–5084. [PubMed: 17962459]
15. Yang H, Downs JC, Girkin C, et al. 3-D Histomorphometry of the Normal and Early Glaucomatous Monkey Optic Nerve Head: Lamina Cribrosa and Peripapillary Scleral Position and Thickness. Invest Ophthalmol Vis Sci 2007;48:4597–4607. [PubMed: 17898283]
16. Downs JC, Yang H, Girkin C, et al. Three Dimensional Histomorphometry of the Normal and Early Glaucomatous Monkey Optic Nerve Head: Neural Canal and Subarachnoid Space Architecture. Invest Ophthalmol Vis Sci 2007;48:3195–3208. [PubMed: 17591889]
17. Chen TC, Cense B, Miller JW, et al. Histologic correlation of in vivo optical coherence tomography images of the human retina. Am J Ophthalmol 2006;141:1165–1168. [PubMed: 16765704]
18. Blumenthal EZ, Parikh RS, Pe'er J, et al. Retinal nerve fibre layer imaging compared with histological measurements in a human eye. Eye. 2007
19. Toth CA, Birngruber R, Boppart SA, et al. Argon laser retinal lesions evaluated in vivo by optical coherence tomography. Am J Ophthalmol 1997;123:188–198. [PubMed: 9186124]
20. Toth CA, Narayan DG, Boppart SA, et al. A comparison of retinal morphology viewed by optical coherence tomography and by light microscopy. Arch Ophthalmol 1997;115:1425–1428. [PubMed: 9366674]
21. Anger EM, Unterhuber A, Hermann B, et al. Ultrahigh resolution optical coherence tomography of the monkey fovea. Identification of retinal sublayers by correlation with semithin histology sections. Exp Eye Res 2004;78:1117–1125. [PubMed: 15109918]
22. Abbott CJ, McBrien NA, Grunert U, Pianta MJ. Relationship of the optical coherence tomography signal to underlying retinal histology in the tree shrew (Tupaia belangeri). Invest Ophthalmol Vis Sci 2009;50:414–423. [PubMed: 18708623]
23. Ruggeri M, Wehbe H, Jiao S, et al. In vivo three-dimensional high-resolution imaging of rodent retina with spectral-domain optical coherence tomography. Invest Ophthalmol Vis Sci 2007;48:1808–1814. [PubMed: 17389515]

24. Gloesmann M, Hermann B, Schubert C, Sattmann H, Ahnelt PK, Drexler W. Histologic correlation of pig retina radial stratification with ultrahigh-resolution optical coherence tomography. Invest Ophthalmol Vis Sci 2003;44:1696–1703. [PubMed: 12657611]
25. Kagemann L, Ishikawa H, Wollstein G, et al. Ultrahigh-resolution spectral domain optical coherence tomography imaging of the lamina cribrosa. Ophthalmic Surg Lasers Imaging 2008;39:S126–131. [PubMed: 18777881]
26. Inoue R, Hangai M, Kotera Y, et al. Three-dimensional high-speed optical coherence tomography imaging of lamina cribrosa in glaucoma. Ophthalmology 2009;116:214–222. [PubMed: 19091413]
27. Burke D. A modification for the combined staining of cells and fibers in the nervous system. Am J Med Technol 1968;34:667–670. [PubMed: 4177722]
28. Strouthidis NG, Yang H, Downs JC, Burgoyne CF. Comparison of Clinical and Three-Dimensional Histomorphometric Optic Disc Margin Anatomy. Invest Ophthalmol Vis Sci 2009;50:2165–2174. [PubMed: 19136694]
29. Strouthidis NG, Yang H, Fortune B, Downs JC, Burgoyne CF. Detection of Optic Nerve Head Neural Canal Opening within Histomorphometric and Spectral Domain Optical Coherence Tomography Data Sets. Invest Ophthalmol Vis Sci 2009;50:214–223. [PubMed: 18689697]
30. Drexler W, Fujimoto JG. State-of-the-art retinal optical coherence tomography. Prog Retin Eye Res 2008;27:45–88. [PubMed: 18036865]
31. Anderson DR, Hoyt WF. Ultrastructure of intraorbital portion of human and monkey optic nerve. Arch Ophthalmol 1969;82:506–530. [PubMed: 4981187]
32. Marshall J, Hamilton AM, Bird AC. Histopathology of ruby and argon laser lesions in monkey and human retina. A comparative study. Br J Ophthalmol 1975;59:610–630. [PubMed: 812546]
33. Emery JM, Landis D, Paton D, Boniuk M, Craig JM. The lamina cribrosa in normal and glaucomatous human eyes. Trans Am Acad Ophthalmol Otolaryngol 1974;78:OP290–297. [PubMed: 4825057]
34. Quigley HA, Hohman RM, Addicks EM, Massof RW, Green WR. Morphologic changes in the lamina cribrosa correlated with neural loss in open-angle glaucoma. Am J Ophthalmol 1983;95:673–691. [PubMed: 6846459]
35. Yan DB, Coloma FM, Metheetrairut A, Trope GE, Heathcote JG, Ethier CR. Deformation of the lamina cribrosa by elevated intraocular pressure. Br J Ophthalmol 1994;78:643–648. [PubMed: 7918293]
36. Povazay B, Bizheva K, Hermann B, et al. Enhanced visualization of choroidal vessels using ultrahigh resolution ophthalmic OCT at 1050 nm. Opt Express 2003;11:1980–1986. [PubMed: 19466083]
37. Povazay B, Hermann B, Unterhuber A, et al. Three-dimensional optical coherence tomography at 1050 nm versus 800 nm in retinal pathologies: enhanced performance and choroidal penetration in cataract patients. J Biomed Opt 2007;12:041211. [PubMed: 17867800]
38. Wang Y, Nelson J, Chen Z, Reiser B, Chuck R, Windeler R. Optimal wavelength for ultrahigh-resolution optical coherence tomography. Opt Express 2003;11:1411–1417. [PubMed: 19466013]
39. Yang H, Downs JC, Burgoyne CF. Physiologic Intereye Differences in Monkey Optic Nerve Head Architecture and Their Relation to Changes in Early Experimental Glaucoma. Invest Ophthalmol Vis Sci 2009;50:224–234. [PubMed: 18775866]

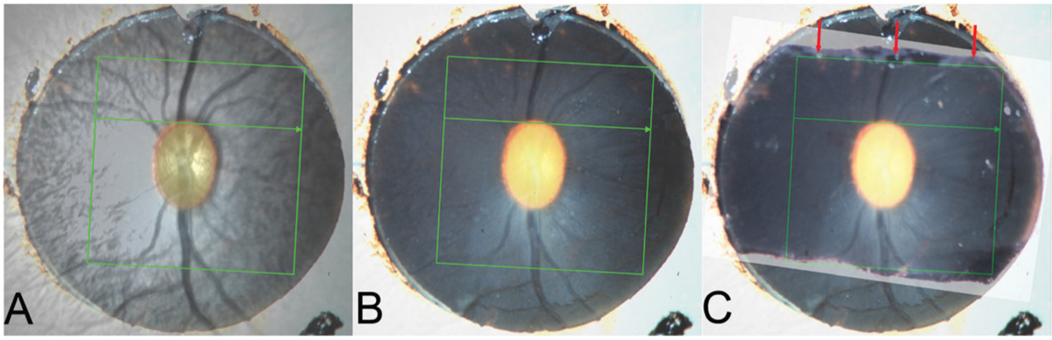

Figure 1. Cutting the optic nerve head trephine in the orientation of the acquired B-scan

A – The SD-OCT IR image including the 15°-acquisition box, viewed at 50% opacity, has been aligned to an image of the optic nerve head trephine.

B – The coordinates of the acquisition box have been burnt onto the trephine image

C – Cuts have been made in the trephine, in an attempt to get the closest approximation to the orientation of the acquired B-scans. The cut made in the superior part of the trephine (red arrows) most closely matches the acquired B-scan orientation. The trephine was embedded with the superior cut surface facing downwards.

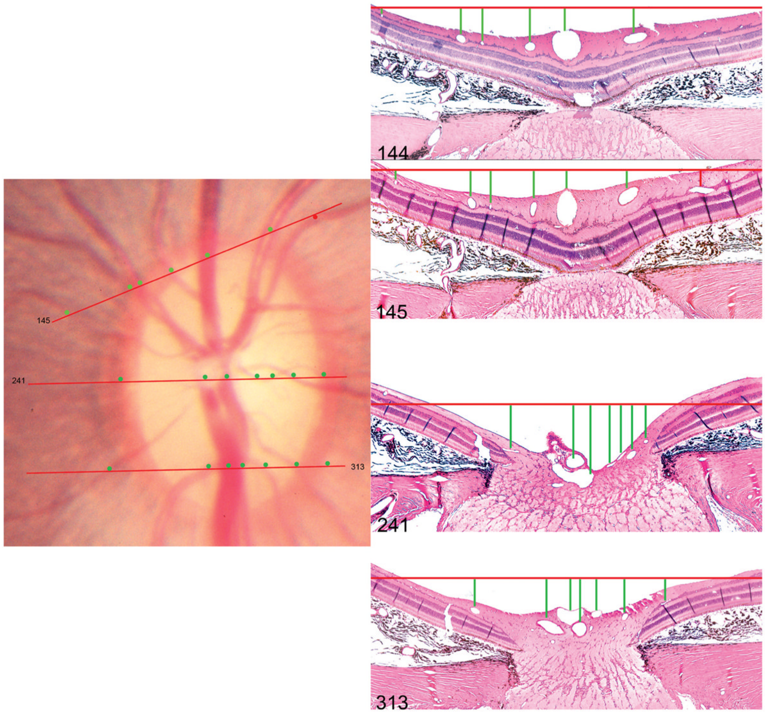

Figure 2. Method of orientating histologic sections to the disc photograph

The topographic locations of histologic sections 145, 241 and 313 (hematoxylin and eosin, X10 magnification) are shown. The orientation of each section (red lines in the disc photograph) is judged by assessing the relative spacing of the retinal vessels, marked by circular glyphs in the disc photograph and by vertical lines in the histologic sections. Note the temporal vessel highlighted by a red glyph is absent in section 144 but appears in the next section (145). The superior opening in Bruchs Membrane (superior disc margin) was identified to be near Section 145 (described in detail in Figure 5) and the inferior opening in Bruch's Membrane was identified to be near to Section 335 (not shown in this figure but described in detail in Figure 6).

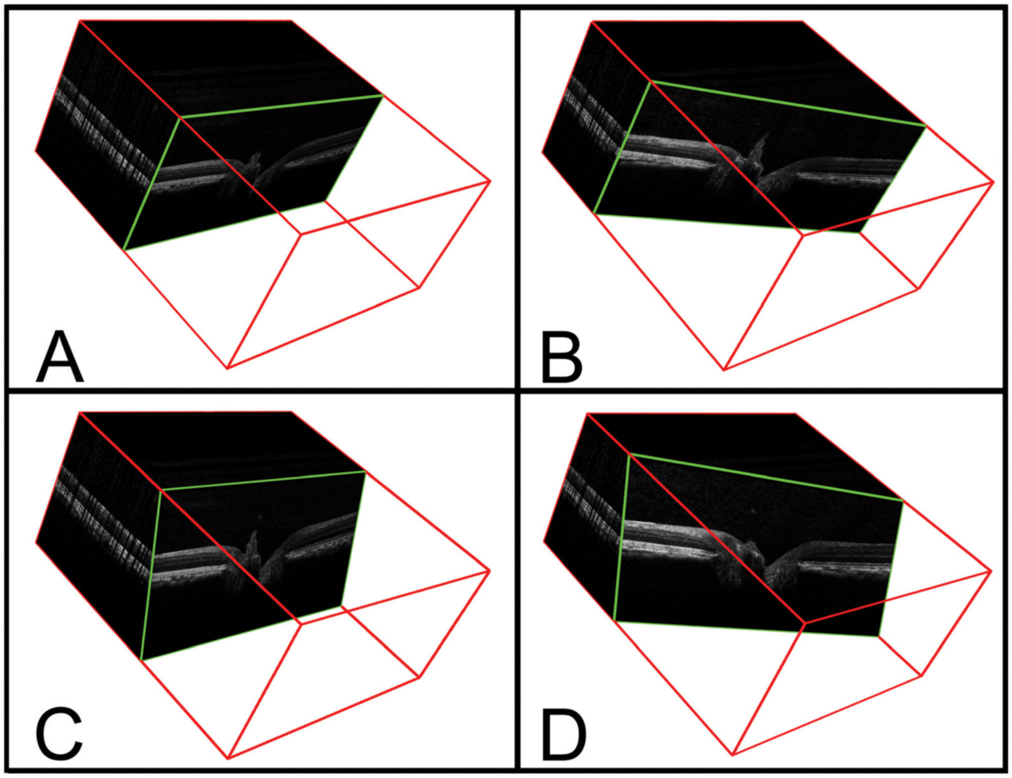

Figure 3. Method of identifying interpolated B-scans from the SD-OCT volumetric reconstruction

A – A representative acquired B-scan is shown within the 3D volume (enclosed within a red cube) generated from a 290 × 768 horizontal raster scan. The angle of rotation of the B-scan is 90° and the angle of incidence is 0°.

B – The interpolated B-scan shown has been generated following a 20° clockwise rotation (angle of rotation = 70°); the angle of incidence is unchanged,

C – The interpolated B-scan shown has been generated following a −20° change in the angle of incidence.

D – The interpolated B-scan shown has been generated using an angle of rotation of 70° and an angle of incidence of −20°.

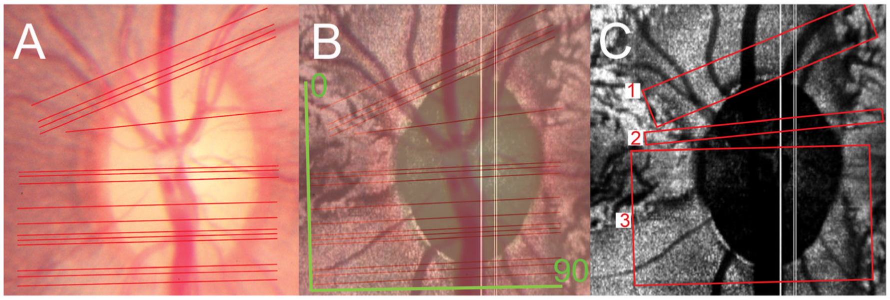

Figure 4. Method of identifying the B-scan angle of rotation

A – The topographic orientation of serial hematoxylin and eosin stained sections is depicted as a series of red lines in the disc photograph. There is a minimum separation of 16 μm between sections. Sections which could not be orientated because of poorly preserved retina account for the variable width of gaps between the lines.

B – The image shown in figure A (viewed at 50% opacity) has been co-localized to the en face SD-OCT image (C-scan). The 0° and 90° orientations of the actual acquired horizontal raster B-scans are shown in green.

C – The angle of rotation of the histologic sections is assessed relative to that of the acquired B-scans varies within three regions; 73.5° in histologic sections from region 1, 87° in histologic sections from region 2 and 89° in histologic sections from region 3.

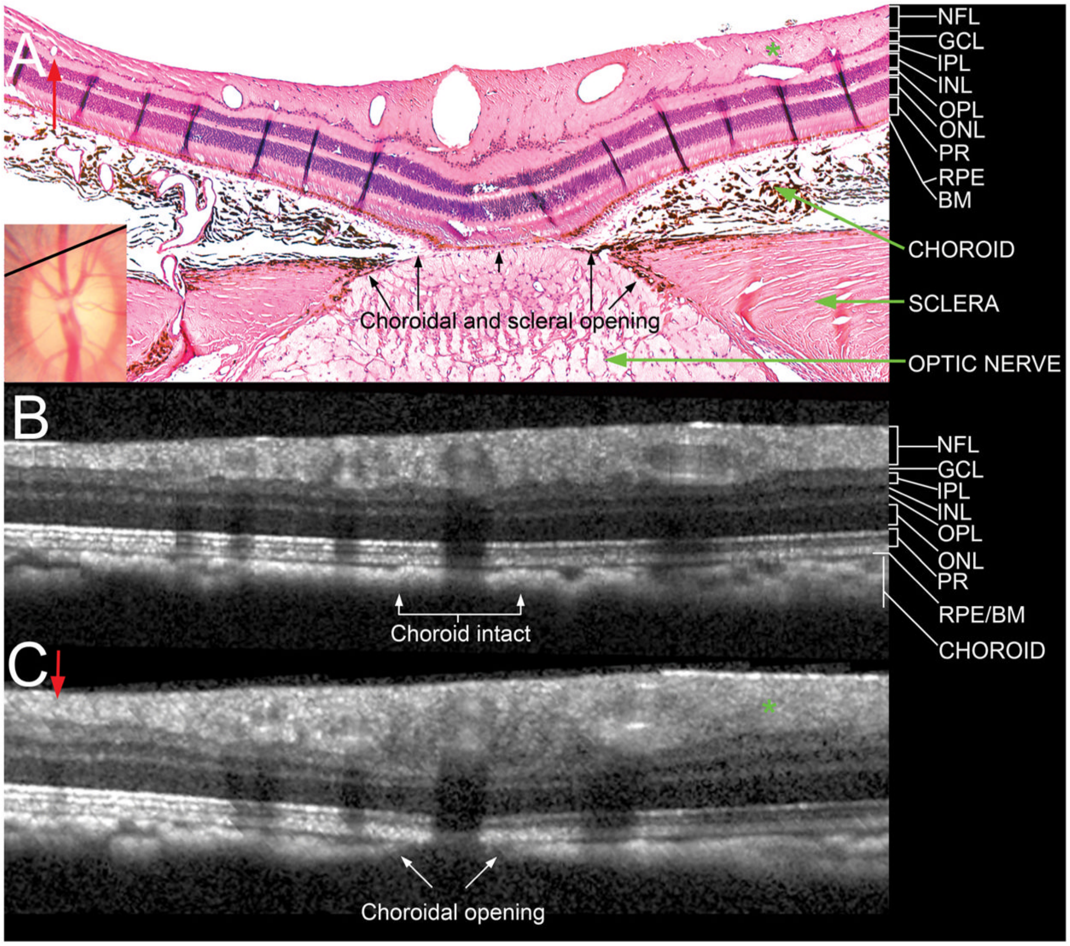

Figure 5. Comparison of a histologic section located near the superior Bruch's membrane opening (disc margin) with matched interpolated B-scans

A – Section 145 (hematoxylin and eosin, X10 magnification) is shown with its topographical location shown as a black line in the disc photograph (inset, also shown in Figure 2). Note the presence of a small vessel in the nasal (left) part of the section, labeled with a red arrow, and an oblique vessel in the temporal (right) part of the section, labeled with a green asterisk. There is an opening in the choroid and sclera but the RPE and Bruch's membrane are intact over the optic nerve.

B – An interpolated section generated from the same topographic location, at an angle of rotation of 73.5°, but with an angle of incidence of 0° (perpendicular to the surface). Note that neither of the vessels highlighted in A are detected and that the choroidal signal appears to be continuous.

C – An interpolated B-scan generated from the same location as B, but with an angle of incidence of −18° (angled towards the nerve). Note that the two vessels are now visible in the correct location (labeled with a red arrow and a green asterisk). An opening in the choroid is now visible, the RPE/BM complex remains intact, but no signal from the deeper optic nerve and lamina cribrosa are detected.

NFL = nerve fiber layer
GCL = ganglion cell layer
IPL = inner plexiform layer
INL = inner nuclear layer
OPL = outer plexiform layer

ONL = outer nuclear layer
PR = photoreceptor layer
RPE/BM = retinal pigment epithelium/Bruch's membrane complex

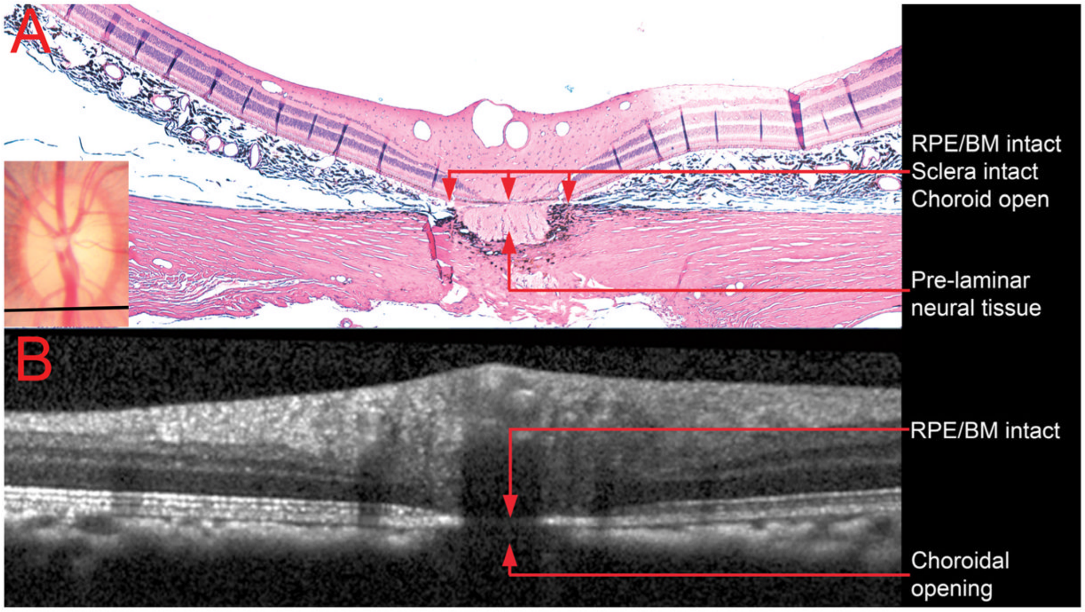

Figure 6. Comparison of a histologic section located near the inferior Bruch's membrane opening (disc margin) with its matched interpolated B-scan

A – Section 335 (hematoxylin and eosin, X10 magnification) is shown with its topographical location depicted shown as a black line in the clinical photograph (inset)

B – The matched interpolated B-scan has been acquired at an angle of rotation of 89°, but the angle of incidence was kept at 0°. Note that the retinal pigment epithelium/Bruch's membrane complex is intact, but the opening in the choroid is present, as in the histologic section. The pre-laminar neural tissue and the intact sclera are most likely not detected because of shadowing from the central retinal vessels.

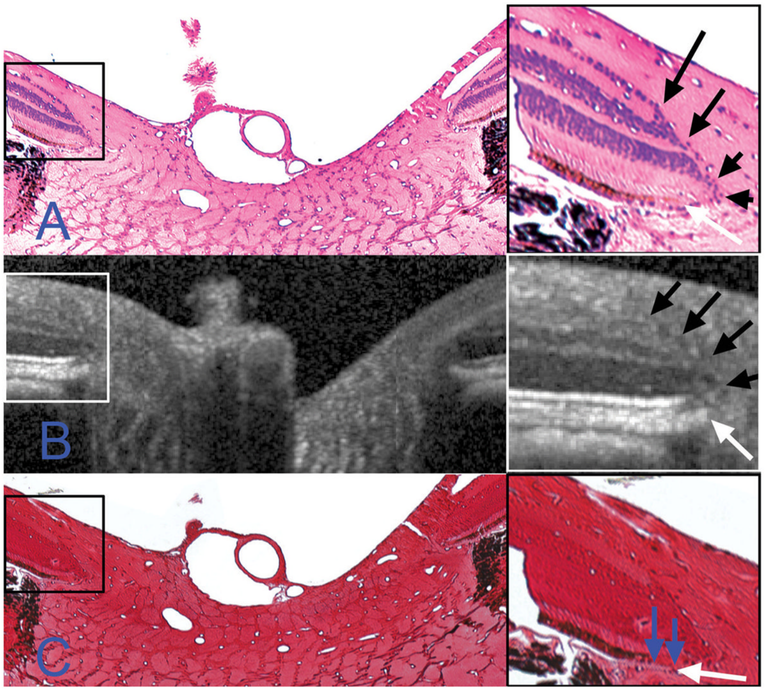

Figure 7. Identification of the neural canal opening. Highlighted regions (boxes on left) are magnified on the right. Note that differences in anterior surface tilt between the B-scan and the histologic sections are likely due to the presence of retinal elevation/detachment and of a 'rip' in the retina on the left hand side of the sections (both features cropped out of A and C). The retinal layers in A and C are as identified in Figure 5

A – Section 257 (hematoxylin and eosin, X10 magnification) is shown. The termination of Bruch's membrane (the neural canal opening) is highlighted with a white arrow in the magnified view. Note that at this location the retinal layers taper to a point (black arrows) at the photoreceptor layer, internal to the NCO.

B – The matched interpolated B-scan. The same relationship between the retinal layers (black arrows) and the termination of the retinal pigment epithelium/Bruch's membrane complex (white arrow) as was detected in A are seen in the magnified view.

C – Section 260 (Ponceau S, X10 magnification). Using this stain, the distinction between the termination of the retinal pigment epithelium and an extension of unpigmented Bruch's membrane (blue arrows) is clearly visible.

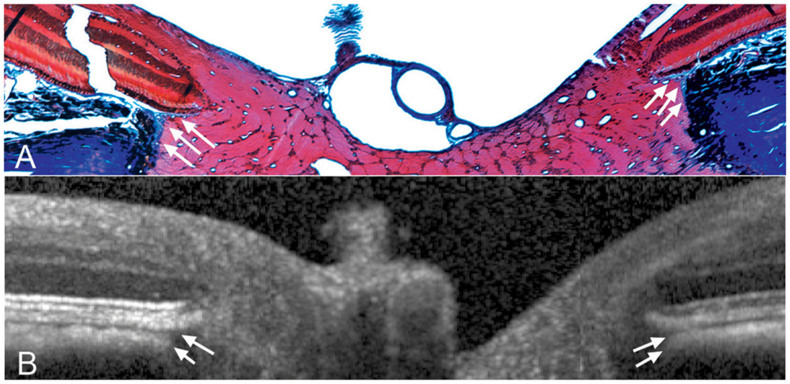

Figure 8. Detection of Border Tissue of Elschnig

A – Section 258 (masson trichrome, X10 magnification), with Border Tissue highlighted with white arrows. This histologic section was located immediately adjacent to the section shown in Figure 7. Note that the Border Tissue of Elschnig is seen as a connective tissue strut (stained blue) connecting the anterior sclera to Bruch's membrane and enclosing the choroid. A more complete view of this section is shown in Figure 9.

B – The Border Tissue signal in the matched interpolated B-scan is highlighted using white arrows. SD-OCT appears to accurately capture the orientation of the Border Tissue with an internally oblique configuration seen nasally (left) and an externally oblique configuration seen temporally (right).[28]

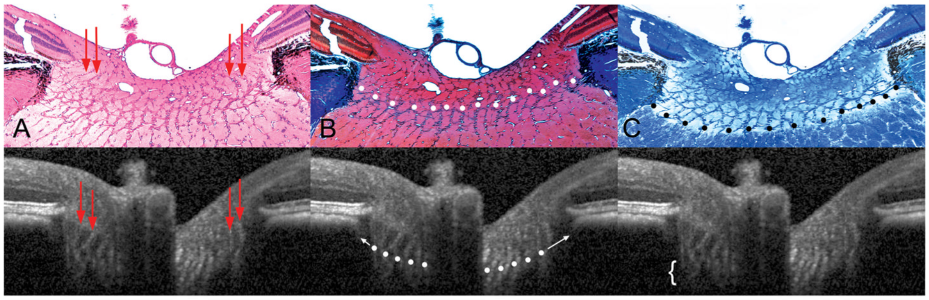

Figure 9. Detection of the lamina cribrosa

A – Section 257 (hematoxylin and eosin, X10 magnification); pre-laminar glial columns appear to correspond to vertical striations seen in the matched interpolated B-scan below (marked with red arrows).

B – Section 258 (masson trichrome, X10 magnification); the anterior lamina surface is delineated with white glyphs. Note that the peripheral insertion of the lamina is not clearly visible in the interpolated B-scan, although the approximate level of insertion may be ascertained by following the contour of the anterior laminar signal to the periphery of the neural canal (white arrows).

C – Section 256 (luxol fast blue, X10 magnification); the posterior lamina surface is delineated with black glyphs in the histologic section. The posterior surface is not detectable in the matched interpolated B-scan, as the signal fades rather than comes to a discrete termination (region highlighted by a white bracket).